Int. J. Plasma Environ. Sci. Technol. 17 (2023) e02001 (13pp)

International Journal of
Plasma Environmental Science and Technology

Regular Paper

DOI: 10.34343/ijpest.2023.17.e02001

Fundamental characteristics of single dielectric barrier discharge plasma actuator using magnetic fluid

Takuya Kuwahara[*], **Yusuke Asaka**

Department of Mechanical Engineering, Nippon Institute of Technology, Japan

[*] Corresponding author: takuya.k@nit.ac.jp (Takuya Kuwahara)

Received: 14 December 2022
Revised: 18 May 2023
Accepted: 24 May 2023

Abstract

A single dielectric barrier discharge (DBD) plasma actuator using magnetic fluid (MF), termed “MF-DBD plasma actuator,” is proposed and developed. The MF-DBD plasma actuator can be applied to fanless air purification devices that can collect low-resistive particulate matter, such as diesel particulate by electrostatic force without re-entrainment. The mechanism of ionic wind generation in the MF-DBD plasma actuator is discussed based on the mechanism in conventional DBD plasma actuators. Ionic wind, temperature distribution, ozone, and ion concentrations are investigated to obtain the fundamental characteristics of the MF-DBD plasma actuator. Consequently, the brightness and length of the nonthermal plasma (NTP) discharge increase with an increase in the input voltage to the high-voltage AC power supply. The positive values of the discharge voltage and current are greater than the negative absolute values. This phenomenon can be explained using the ionic wind generation mechanism. A spike movement on the MF surface is observed. Based on the temperature analysis, natural convection occurs inside the MF and convection suppresses the temperature increase of the MF by self-cooling. The characteristics of ion wind velocity with respect to the input voltage and discharge current are similar to those of conventional DBD plasma actuators. The relationship between ozone concentration and the input voltage is clarified. Based on ion concentration measurements, negative ion concentration is extremely low overall. The characteristic of positive ions with respect to the input voltage is obtained.

Keywords: Nonthermal plasma, magnetic fluid, dielectric barrier discharge, ozone, ionic wind.

---

1. Introduction

A magnetic fluid (MF) filter aided with nonthermal plasma (NTP) has been developed [1]. An MF is a colloidal solution comprising fine ferromagnetic particles, with a typical size of 10 nm, suspended stably in a solvent using surfactants. The fluid is magnetized in a magnetic field. In other words, the MF behaves like a magnetizable liquid. In this filter, an MF is fixed to one electrode on one side of the dielectric barrier discharge (DBD) with a magnet, and plasma discharges from spikes generated on the top surface of the MF by applying a high AC voltage. Ozone generation characteristics produced by DBD from MF spikes was investigated [2]. Because the MF is fixed with a magnet, the MF filter with NTP can be used either horizontally or vertically, regardless of its position. Moreover, particulate matter (PM) collections based on the electrostatic force are effective for a wide range of particle sizes. However, PM collections using the electrostatic force are faced with the inherent problem of low-resistance PM losing its charges at the collection electrode and re-scattering into the main flow [3, 4]. This re-entrainment results in the poor collection. The MF filter with NTP resolves the problem of re-entrainment by adsorbing and collecting PM onto the surface of the MF. This filter is advantageous in that it can collect low-resistive PM, such as diesel particulate by electrostatic force without re-entrainment.

PM collection without mechanical fans, that is, a fanless PM collection is attractive for further development of the MF filter with NTP for air purification devices. A possibility for a fanless PM collection is the utilization of ionic wind (ion or electric wind). One example of a fanless PM collection device using MF and NTP is illustrated in Fig. 1, which depicts the principle of PM collection and the electrodes configuration. The ionic wind generated by DBD plasma actuators using MF can introduce pollutant gas containing PM. In addition, pre-treatment for PM collection by electrostatic forces can be achieved through the charging of particulate matter via NTP discharge from the DBD plasma actuators using MF. Although the development of the fanless PM collection device remains a subject for future work, the elucidation of the fundamental characteristics of a DBD plasma actuator using MF is of interest. Hauksbee reported the phenomenon of ionic wind in 1709 [5]. This is the discovery of ionic wind [6]. Ionic wind can be induced using plasma actuators. A plasma actuator that uses the NTP and electrohydrodynamic (EHD) phenomenon can induce or control internal and external flows. DBD and corona discharges are mainly used as discharge methods for the ionic wind [7, 8]. The DBD plasma actuator is crucial in this study. DBD plasma actuators and their ionic wind generation mechanisms have been extensively studied both theoretically [9, 10] and experimentally [11−13]. The plasma actuator has a simple structure, a small number of components, and easy flow control, making it advantageous. Therefore, the plasma actuator and ionic wind are used in various applications, such as aerofoil [14, 15], fan, blower [16], and air purification [17]. The DBD plasma actuator has also been improved to efficiently generate ion wind [18]. The effect of the applied electric waveform on the ion wind velocity has been investigated to understand the ionic wind mechanism [19, 20].

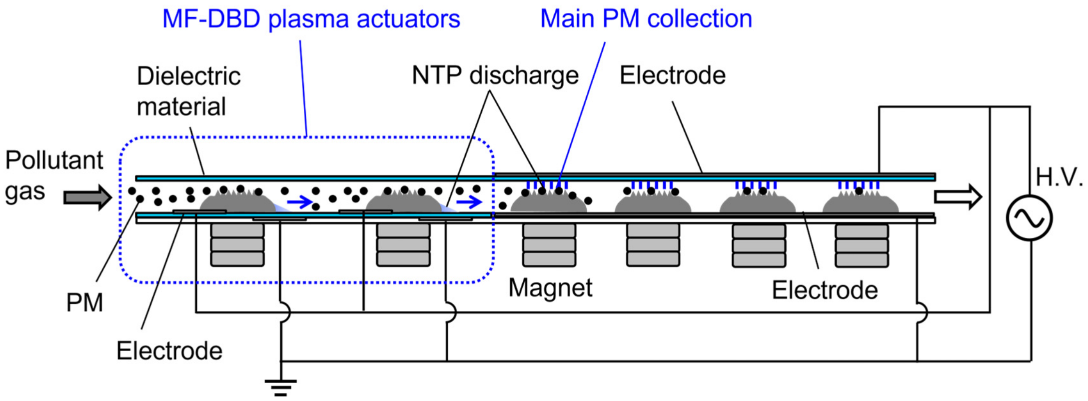

Fig. 1. Principle of fanless PM collection device using MF and NTP.

A DBD plasma actuator using MF in view of DBD plasma actuators and MF filter with NTP is proposed, termed “magnetic fluid DBD (MF-DBD) plasma actuator. To obtain the fundamental characteristics, a single MF-DBD plasma actuator with a simple and fundamental structure is designed and established in this study. In the case of air purification, the ionic wind introduces the gas or air to be purified into the MF-DBD plasma actuator. Relatively large PMs can be adsorbed and collected on the surface of the MF owing to inertia and gravity. In addition, by arranging multiple MF-DBD plasma actuators, PMs with a wide range of diameters can be charged by discharge and they are collected on other MF surfaces. Furthermore, ozone generated by NTP discharge is effective for sterilization and deodorization in air purification. Thus, the fundamental characteristics of the MF-DBD plasma actuator, such as ionic wind, temperature distribution, and ozone concentration are investigated.

2. Experimental

2.1 Principle of single MF-DBD plasma actuator

An MF or ferrofluid is a colloidal solution comprising fine ferromagnetic particles, with a typical size of 10 nm, suspended in solvent using surfactants. The fluid is magnetized in a magnetic field. Magnetite (Fe_3O_4) is commonly used for ferromagnetic particles, which are coated with surfactants. The hydrophilic end of the surfactant attaches to the surface of the ferromagnetic particle, whereas the hydrophobic end attaches to an oil-based solvent (such as kerosene). The surfactant prevents the aggregation of ferromagnetic particles. In a water-based MF, a double layer of surfactants is coated on the ferromagnetic particles. Spiking is a unique phenomenon exhibited by MFs in which spikes form along the magnetic field lines. Further, the pattern, density, and length of the spikes can be controlled by controlling the magnetic flux density. The formation of spikes is an interfacial phenomenon observed if the magnetic flux density exceeds a critical value [21]. For example, for a water-based MF (W-40, Ichinen Chemicals Co., Ltd.), the theoretical critical magnetic flux density is $B_c = 86.6 \times 10^{-4}$ T [22].

The DBD is an NTP discharge achieved by inserting a dielectric material between high-voltage electrodes. In general, A high AC voltage is applied to the electrodes. A surface DBD is a type of DBD [23]. In a surface DBD, the electrodes are in direct contact with a dielectric material. In most cases, DBD plasma actuators utilize the surface DBD. The MF-DBD plasma actuator is also the surface DBD type. The principle of ionic wind generation in the MF-DBD plasma actuator is shown in Fig. 2. The electrodes and dielectric material are placed to be the surface DBD type. The magnets are used to fix the MF on the exposed electrode as shown in Fig. 2. Spikes occur on the surface of the MF. The MF functions as an electrode; that is, as an MF electrode. The MF and the insulated electrode sandwich the dielectric material. In this configuration, NTP discharge occurs on the surface of the dielectric material from the edge of the MF when a high AC voltage is applied to the exposed and insulated electrodes. The ionic wind is induced by the NTP discharge

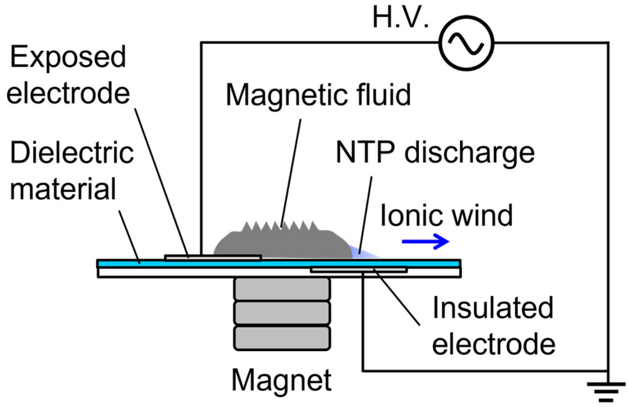

Fig. 2. Principle of ionic wind generation in the MF-DBD plasma actuator.

The ionic wind is induced by a collision between the drifting ions and the neutral particles in the gap of electrodes. Ionic wind velocity u owing to EHD is proportional to the square root of current i [24].

$$u = k_1 \sqrt{i} \quad . \tag{1}$$

Expanding Eq. (1), the ionic wind velocity u is formulated as follows [25, 26]:

$$u = \sqrt{\frac{iD}{\rho_g \mu_i A}} = \sqrt{\frac{jD}{\rho_g \mu_i}} \tag{2}$$

where D is the gap between electrodes, ρ_g is the gas density, μ_i is the ionic mobility, A is the discharge cross section, and j is the time-averaged discharge current density. In particular, Eq. (2) is applied to an ionic wind velocity produced by a corona discharge. In addition, the ionic wind velocity is proportional to the applied voltage [24]. The ionic wind generation mechanism in the MF-DBD plasma actuator is similar to that of the DBD plasma actuator. The mechanism of ionic wind generation in the MF-DBD plasma actuator is shown in Fig. 3. Based on the mechanism in conventional DBD plasma actuators [13], in MF-DBD plasma actuators, dielectric breakdown of the air occurs when a high AC voltage is applied. The air becomes a plasma state with electrons and positive ions. The collision of electrons with air immediately produces negative ions as well. The polarity of the MF electrode on the dielectric material changes periodically. In the case in which the MF electrode is negative, as shown in Fig. 3 (a), the electrons are emitted by the electrostatic force from the MF electrode toward the insulated electrode underneath the dielectric material. However, owing to a dielectric layer, the discharge terminates on the dielectric surface. Thus, electrons accumulated on the dielectric layer as shown in Fig. 3 (b). In Fig. 3 (a), the negative ions also contribute to the generation of ionic wind [27]. In the case in which the MF electrode is positive, as shown in Fig. 3 (c), electrons accumulated on the dielectric layer travel toward the MF electrode. Notably, the discharge for negative and positive voltages is asymmetrical because of the different electrode geometries between the MF electrode and the insulated electrode underneath the dielectric material. as shown in Figs. 3 (b) and (d). In the case in which the MF electrode is positive as shown in Fig. 3 (c), the electrons accumulated on the dielectric surface in Fig. 3 (b) also contribute to the motion. As a result, the total momentum of the electrons in Fig. 3 (c) is greater than the total momentum in the case in which the MF electrode is negative as shown in Fig. 3 (a). The positive ions, paired with electrons and negative ions, have an inverse behavior compared with the electrons and negative ions. Electrons move to the electrode in a very short time owing to their high mobility. In this state, the positive ions remain. The drifting ions collide with the neutral particles. The ionic wind is induced by this collision that transfers momentum to the neutral particles.

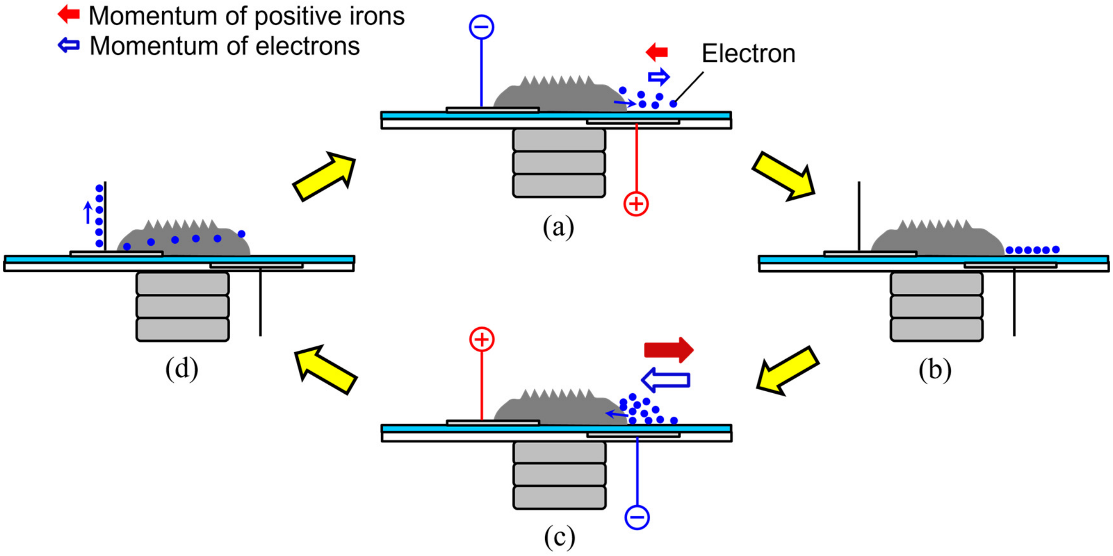

Fig. 3. Mechanism of ionic wind generation in the MF-DBD plasma actuator. (a) The exposed electrode is negative. (b) The exposed electrode is from negative to positive. (c) The exposed electrode is positive. (d) The exposed electrode is from positive to negative.

Accompanying the NTP discharge, ozone is generated from oxygen contained in the air based on the following chemical reactions:

$$O_2 + e \rightarrow O + O + e, \qquad (3)$$

$$O + O_2 \rightarrow O_3. \qquad (4)$$

Ozone is effective for sterilization and deodorization in air purification. Therefore, ozone concentration produced in the single MF-DBD plasma actuator is crucial.

2.2 Experimental setup and measurement

The schematic of the single MF-DBD plasma actuator and its photograph are shown in Fig. 4, according to which the dimensions and the ionic wind velocity measurement point are presented. The magnetic flux density on the surface of the permanent magnet (a set of three neodymium magnets) is 490 mT. A water-based MF (W-40, Ichinen Chemicals Co., Ltd.) is retained by the magnetic field of the permanent magnets. The mass of the MF is 3.6 g. In this configuration, spikes are formed on the top surface of the MF, as shown in the photograph of Fig. 4. The spike has a square bottom (generally 2 mm × 2 mm) and a height of 1.5–2.0 mm. A glass plate is used as the dielectric material. The gap between the cover plate and the MF spike is approximately 2 mm. Aluminum tape is used for the exposed and insulated electrodes. Other walls and the top cover plate are made of acrylic material. The cover plate is removable.

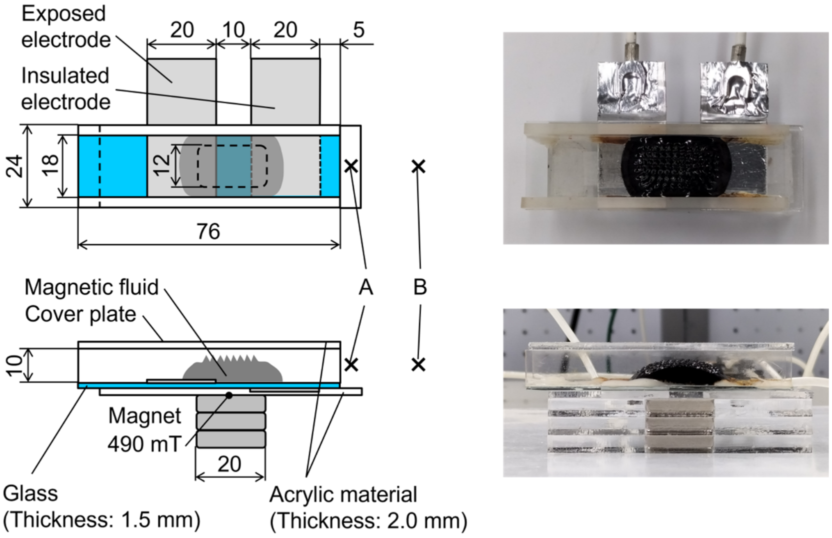

Fig. 4. Schematic of a single MF-DBD plasma actuator and its photograph.

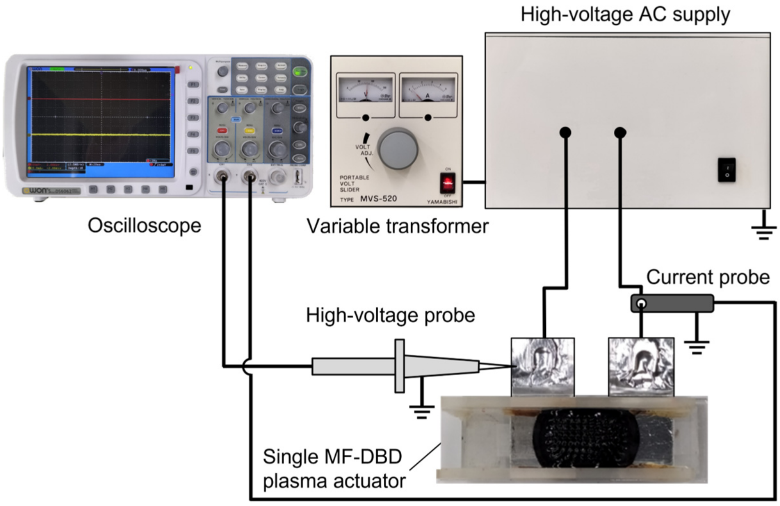

Fig. 5. Experimental setup of the single MF-DBD plasma actuator and electrical connection.

The experimental setup of the single MF-DBD plasma actuator and electrical connection is shown in Fig. 5. The high AC voltage is applied to the electrodes using a high-voltage AC power supply (LHV-13AC, Logy Electric Co., Ltd.) with a production capacity of 10 kV at 9 kHz. The input power to the power supply is provided by a variable voltage transformer (MVS520, Yamabishi Denki) such that the input voltage can be regulated. The measurement items are ionic wind velocity, temperature distribution, ozone concentration, power consumption, and discharge voltage and current. The ionic wind velocity is measured using a hot wire anemometer (CW-60, Custom Corporation) at the measurement point A (10 mm from the edge of the insulated electrode) in Fig. 4. The temperature distribution is measured with a thermography camera (Hikmicro B20, Hangzhou Microimage Software Co., Ltd.). The cover plate is removed in the temperature distribution measurement for accurate measurement. NTP discharge and MF temperatures are obtained from thermography. Ozone concentration is measured using a gas detector tube (No. 18M, Gastec Corporation) at the same measurement point as the velocity measurement. The power consumption is measured using a wattmeter (TAP-TST7, Sanwa Supply Inc.). The discharge voltage and current are measured using an oscilloscope (DS6062, Owon Technology Inc.), a high-voltage probe (P6015A, Tektronix Inc.), and a current probe (P6021A, Tektronix Inc.) as shown in Fig. 5. The discharge voltage is measured at the exposed electrode. Positive and negative ion concentrations are measured using an ion counter (NT-C101A, Andes Electric Co., Ltd.) at measurement point B (30 mm from the edge of the insulated electrode) in Fig. 4. The ion counter is equipped with a double coaxial cylinder type ion detection sensor. Measured values are calculated using a conversion formula based on the Japanese Industrial Standards (JIS) B 9929.

3. Results and discussion

3.1 NTP discharge characteristics

The resultant NTP discharge, i.e. DBD with respect to the input voltage are shown in Fig. 6. The photographs of DBD with respect to the input voltage are shown in Fig. 6 (a). The resultant photographs at the input voltage V_{in} = 40−100 V to the high-voltage AC power supply are presented. Consequently, no NTP discharge is observed at V_{in} = 0−40 V; however, it is observed at V_{in} = 50−100 V. NTP micro-discharges are generated from the edge surface of the MF toward the insulated electrode. As the input voltage increases, the brightness and length of the NTP discharge increase. Therefore, as the input voltage increases, the discharge current increases. Discharging from an MF can prevent the exposed electrode from being damaged by the discharge. Fig. 6 (b) shows the relationship between input voltage V_{in} and discharge area A_{dis} by image processing. An example of image processing at V_{in} = 100 V is also shown in the graph. The graph also shows an approximated line. The image processing procedure is as follows: First, the reference area of 12.2 mm ×18.0 mm containing the discharge is cropped and converted to grayscale. The grayscale image has 256 shades of gray in a pixel. To count the pixels of discharge area, the number of pixels in 150−255 shades is counted. The discharge area is calculated based on the number of pixels and area of the reference area. The graph shows that as V_{in} increases, the discharge area also increases.

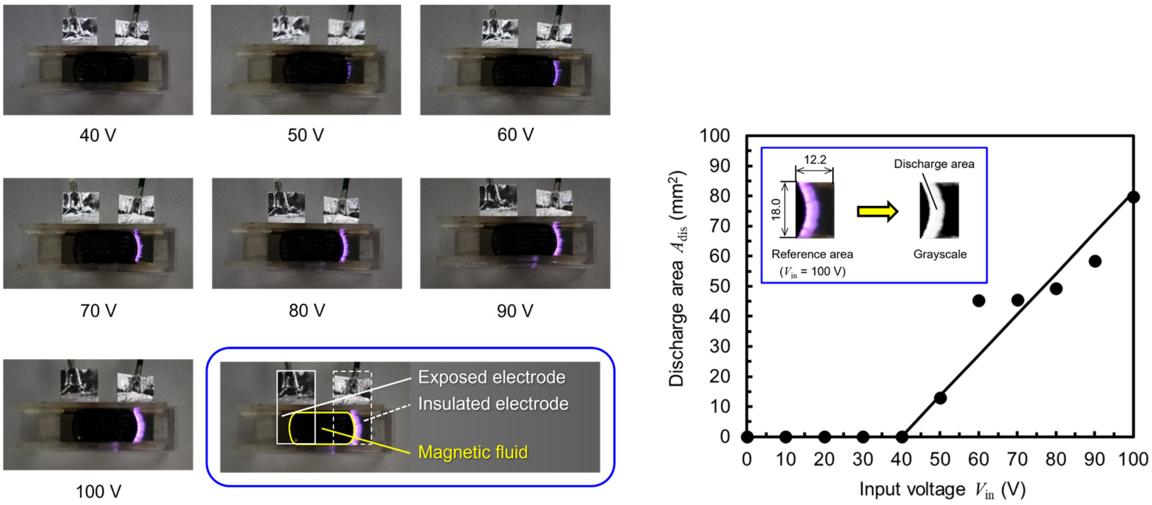

(a) (b)

Fig. 6. The resultant NTP discharge, i.e. DBD with respect to the input voltage. (a)Photographs of NTP discharge with respect to input voltage V_{in}. (b) Relationship between input voltage V_{in} and discharge area A_{dis} by image processing.

The relationship between the input voltage V_{in} and the power consumption P_{con} at the high-voltage AC power supply is shown in Fig. 7. Data are measured 10 s after turning on the power supply. It is noted that P_{con} includes the power consumed by the internal circuit of the power supply. The data are the average value of six measurements and their standard errors. The standard errors are small. The measured P_{con} is plotted with a solid line that is an approximate curve with squared approximation at V_{in} = 20−100 V. The result is as follows. The approximate curve is expressed at V_{in} = 20−100 V as

$$P_{\mathrm{con}} = \alpha {V_{\mathrm{in}}}^2 \qquad (5)$$

where α is a coefficient (α = 6.5 × 10^{-3} A/V in this study). Notably, the 5 W is consumed initially by the circuit, even without discharge at V_{in} = 0−20 V. Based on this result, although no NTP discharge is observed visually at V_{in} = 0−40 V, a weak NTP discharge can occur even at V_{in} = 30−40 V.

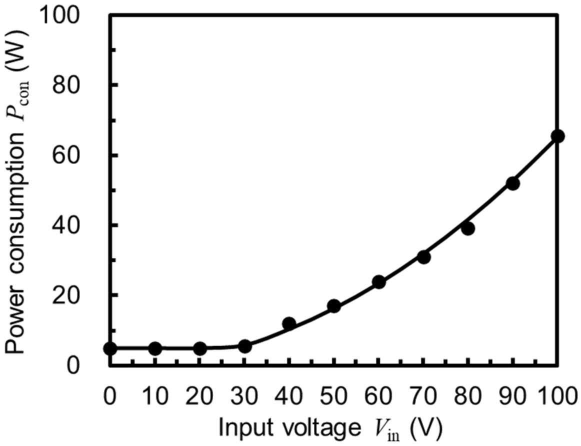

Fig. 7. Relationship between the input voltage V_{in} and the power consumption P_{con} in the high-voltage AC power supply.

The discharge voltage characteristics are shown in Fig. 8. The waveforms of the discharge voltage V_{dis} and current I_{dis} at V_{in} = 100 V are shown in Fig. 8 (a). The waveform of V_{dis} is sawtooth on both the positive and negative sides with a frequency f = 12.8 kHz. In the case of the first cycle, the instantaneous maximum value of the discharge voltage V_{max}, that is, the zero-to-peak voltage $V_{0\text{–}p}$ is 8.8 kV and the minimum value V_{min} is −5.6 kV. The peak-to-peak and root-mean-square (RMS) values of the discharge voltage are $V_{p\text{-}p}$ = 14.4 kV and V_{RMS} = 4.3 kV, respectively. This voltage waveform could be due to the characteristics of the power supply. The instantaneous maximum value of the discharge current I_{max} is 45.6 mA and the minimum value I_{min} is −22.4 mA. The peak-to-peak and RMS values of the discharge current are $I_{p\text{-}p}$ = 68.0 mA and I_{RMS} = 12.2 mA, respectively. A fine waveform with a frequency f_s of approximately 100 kHz overlaps the main sawtooth waveform in the discharge voltage and current. This fine waveform can be caused by the micro-discharges that constitute the DBD. The positive values of the discharge current are greater than the negative absolute values; that is, $|I_{max}| > |I_{min}|$. This is because in the case in which the exposed electrode is negative, although electrons are emitted from this electrode, these electrons are accumulated on the dielectric layer as explained in Figs. 3 (a) and (b). Consequently, the number of flowing electrons decreases and the current decreases as well. However, in the case in which the exposed electrode is positive, the deposited electrons also move toward the exposed electrode, as explained in Figs. 3 (c) and (d). Consequently, the number of flowing electrons increases and the current increases. Relationships between input voltage V_{in} and discharge voltage V_{dis} (V_{RMS} and $V_{0\text{–}p}$) are shown in Fig. 8 (b). The black circle shows the V_{RMS} and the white circle shows the $V_{0\text{–}p}$. The solid line is an approximation.

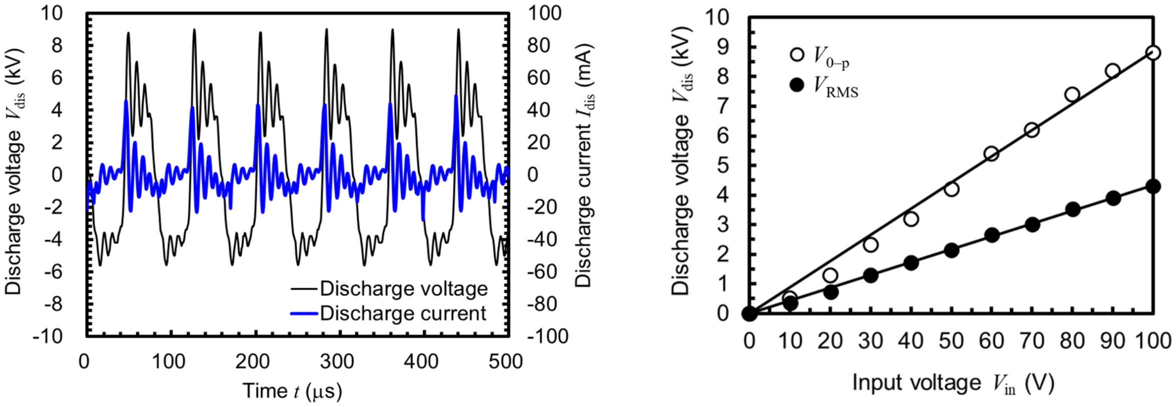

(a) (b)

Fig. 8. Discharge voltage characteristics. (a) Waveforms of discharge voltage V_{dis} and current I_{dis} at V_{in} = 100 V. (b) Relationship between input voltage V_{in} and discharge voltage V_{dis} (RMS V_{RMS} and zero-to-peak $V_{0\text{–}p}$).

A linear relationship exists in both V_{RMS} and $V_{0\text{–p}}$ cases. The linear relationships are expressed as follows:

$$V_{\mathrm{RMS}} = 43.4V_{\mathrm{in}} \tag{6}$$

$$V_{0\text{–p}} = 88.5V_{\mathrm{in}} \tag{7}$$

3.2 Temperature characteristics

The time-dependent temperatures of NTP discharge and MF are shown in Fig. 9 (a). The white circle shows the NTP discharge temperature T_{NTP} and the black circle shows the temperature at the center of the MF T_{MF}. These are the average values of six measurements and their standard errors. The standard errors are small. A solid line indicates a curve approximated by a second-order polynomial. The initial room temperature and humidity are approximately 27 °C and 34%, respectively. Consequently, the T_{NTP} increases abruptly to 61.6 °C in the first 10 s, and then increases gently to 85.7 °C at the elapsed time t =120 s. Conversely, the T_{MF} increases gently to 38.6 °C at t =120 s. The temperature difference $\Delta T = T_{\mathrm{NTP}} - T_{\mathrm{MF}}$ is 34.8 °C in the first 10 s, and then increases slowly to 47.1 °C at t =120 s. The thermography of a single MF-DBD plasma actuator at t =120 s is shown in Fig. 9 (b). Inside the actuator, the NTP discharge temperature (85.8 °C) is the highest, followed by the temperature (approximately 60–70 °C) of the dielectric above the insulated electrode. However, the temperature of the electrodes (approximately 27 °C) does not increase. The high-temperature of the NTP discharge is caused by electrons with high temperature as shown in Figs. 3 (a) and (c). The temperature increase of the dielectric above the insulated electrode results from the high temperature electrons accumulated on the dielectric layer, as shown in Fig. 3 (b).

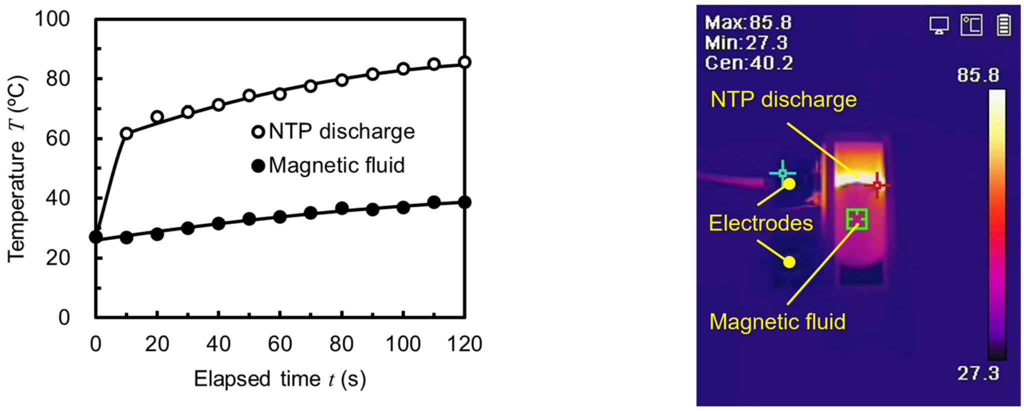

(a) (b)

Fig. 9. Temperature change and distribution. (a) Time-dependent temperatures T of NTP discharge and MF. (b) Thermography of a single MF-DBD plasma actuator at an elapsed time t =120 s.

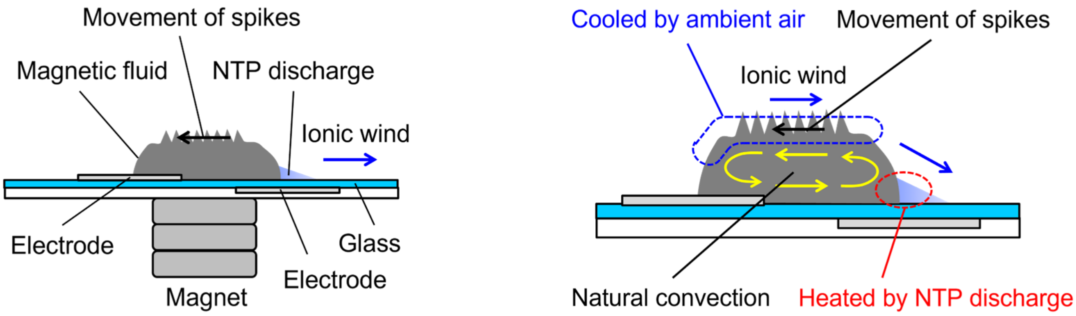

(a) (b)

Fig. 10. Explanation of natural convection in MF. (a) Schematic of movement of spikes on the MF surface and ionic wind flow. (b) Schematic of internal natural convection in the MF and self-cooling.

Accompanying the NTP discharge, the spikes on the surface of the MF move in the direction shown in Fig. 10 (a). A possible mechanism of the spike movement is shown in Fig. 10 (b). The bottom edge of the MF on the side of the insulated electrode is heated by the NTP discharge. The heated MF rises and is cooled by ambient air. This causes natural convection inside the MF. That is, the convection suppresses the temperature increase of the MF by self-cooling as a result of Fig. 10 (b). Cooling by ambient air is enhanced by the formation of spikes on the MF that increase the surface area (the heat-exchange area).

3.3 Characteristics of Ionic wind velocity

The relationship between the input voltage V_{in} and the ionic wind velocity u is shown in Fig. 11 (a). In the measurement, the room temperature and humidity are generally 22 °C and 24%, respectively. Data are measured 10 s after turning on the power supply. The data are the average values of seven measurements and their standard errors. The solid line is an approximation. u is zero at V_{in} = 0−60 V.

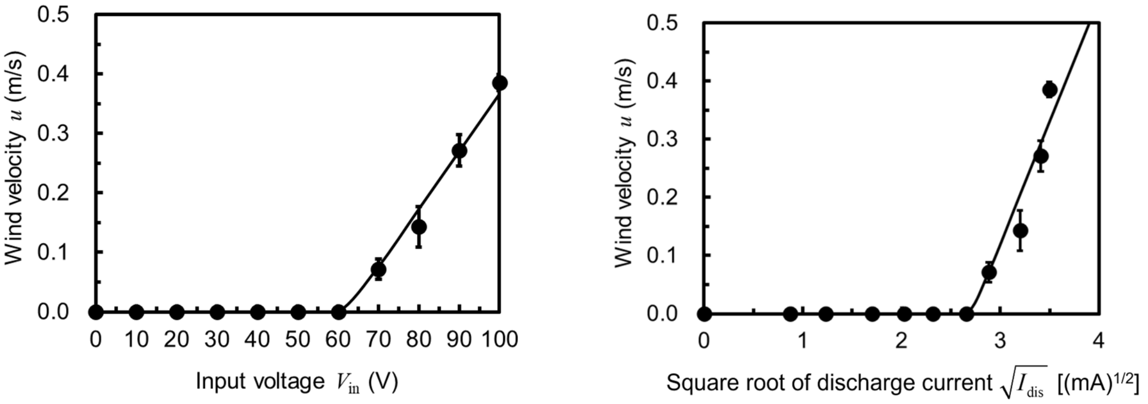

(a) (b)

Fig. 11. Ionic wind velocity characteristics. (a) Relationship between the input voltage V_{in} and the wind velocity u induced by the ionic wind. (b) Relationship between the square root of discharge current $\sqrt{I_{\mathrm{dis}}}$ and the wind velocity u.

A linear relationship exists at V_{in} = 60−100 V. Thus, the ionic wind velocity in a single MF-DBD plasma actuator is proportional to the applied voltage as follows:

$$u = k_2 \Delta V_{\mathrm{in}} = k_2 (V_{\mathrm{in}} - V_0) \tag{8}$$

where k_2 is a coefficient and V_{o} is the input voltage at the start of ionic wind generation. In this experiment, $k_2 = 9.7 \times 10^{-3}$ and V_{o} = 60 V. Considering the discharge voltage V_{dis} (V_{RMS} and $V_{\mathrm{0\text{-}p}}$) in Eqs. (6) and (7), the ionic wind velocity can be rewritten as

$$u = k_3 \Delta V_{\mathrm{RMS}} = k_4 \Delta V_{\mathrm{0-p}} \tag{9}$$

where $k_3 = k_2/43.4 = 2.2 \times 10^{-4}$, ΔV_{RMS} is the differential V_{RMS} from the start of ionic wind generation, $k_4 = k_2 / 88.5 = 1.1 \times 10^{-4}$ and $\Delta V_{\mathrm{0\text{-}p}}$ is the differential $\Delta V_{\mathrm{0\text{-}p}}$ from the start of ionic wind generation. This result agrees with the conventional plasma actuator [24]. Consequently, the ionic wind velocity u is generally 0.4 m s^{-1} at V_{in} = 100 V. Notably, although u is not detected at V_{in} = 0−60 V, a weak ionic wind can occur even at V_{in} = 30−60 V as shown and discussed in the power consumption P_{con} in Fig. 7. Considering Eq. (1) as $i \approx I_{\mathrm{dis}}$, the relationship between the square root of the discharge current $\sqrt{I_{\mathrm{dis}}}$ and the wind velocity u is shown in Fig. 11 (b). The solid line is an approximation. The linear relationship at $\sqrt{I_{\mathrm{dis}}} \geq 2.66$ (mA)$^{1/2}$ is expressed as follows:

$$u = k_1 \Delta \sqrt{I_{\mathrm{dis}}} = k_1 (\sqrt{I_{\mathrm{dis}}} - \sqrt{I_0}) \ . \tag{10}$$

In this experiment, $k_1 = 0.42$ and $I_0 = 2.66$ (mA)$^{1/2}$.

3.4 Characteristics of ozone and ion concentrations

The relationship between the input voltage V_{in} and the ozone concentration C_{O3} produced by the NTP discharge is shown in Fig. 12. In the measurement, the room temperature and humidity are 24 °C and 36%, respectively. The data are measured 10 s after turning on the power supply. The data are the average values of three measurements and their standard errors. A solid line indicates a curve approximated by a third-order polynomial at V_{in} = 50−100 V. C_{O3} is zero at V_{in} = 0−50 V. C_{O3} increases at V_{in} = 60−90 V. C_{O3} is 140 ppm at V_{in} = 90 V. C_{O3} decreases to 113 ppm at V_{in} = 100 V. Ozone is generated through the collision of oxygen molecules and electrons in the air. As the input voltage increases, the number of electrons released by discharge should also increase as seen in Fig. 6 (a), allowing efficient ozone generation at V_{in} = 100 V. However, C_{O3} is observed to be decreasing. Because this decrease in C_{O3} is unlikely to be caused by electrical factors of discharge, this decrease in C_{O3} can result from dilution by air induced by the ionic wind.

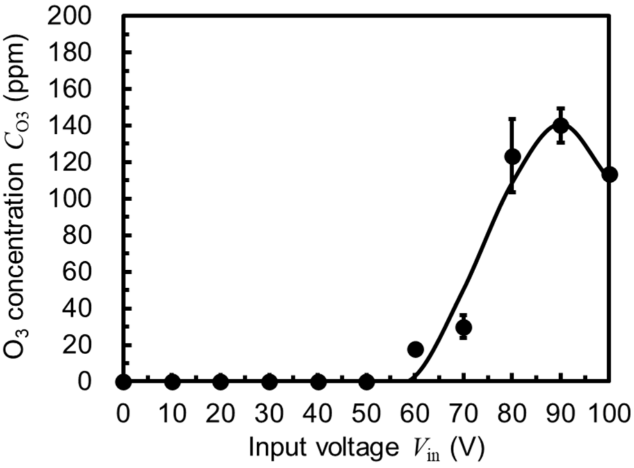

Fig. 12. Relationship between the input voltage V_{in} and the ozone concentration C_{O3}.

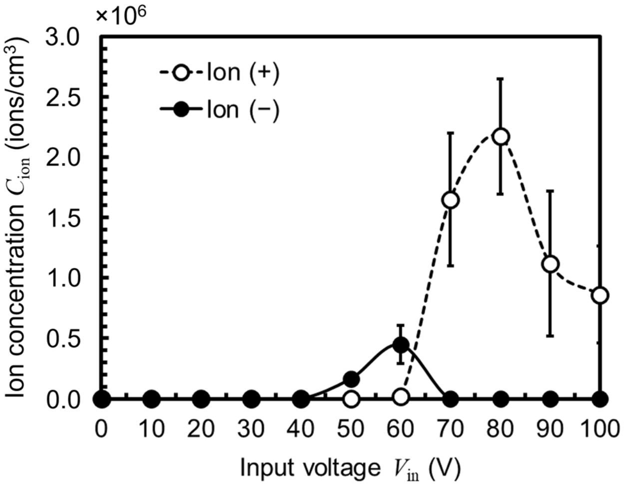

Fig. 13. Relationship between the input voltage V_{in} and the ion concentration C_{ion}.

The relationship between the input voltage V_{in} and the ion concentration C_{ion} produced by NTP discharge is shown in Fig. 13. Negative ions are plotted as black circles and smoothly connected by solid lines. Positive ions are plotted as white circles and smoothly connected by dashed lines. In the measurement, the room temperature and humidity are 22 °C and 37%, respectively. In one measurement, the average of ion concentrations per second for the first 10 s after turning on the power supply is obtained. The data are the average values of six measurements and their standard errors. In the case of negative ions, although the C_{ion}

reaches 0.45×10^6 ions cm^{-3} at $V_{\mathrm{in}} = 60$ V, C_{ion} is extremely low. One possible explanation is that as the strength of the electric field increases, the generated electrons flow back to the MF electrode. in the process of Figs. 3 (c) and (d). Therefore, few electrons are emitted into the atmosphere. The higher negative ion concentration at $V_{\mathrm{in}} = 50{-}60$ V may possibly be because the discharge is weak at $V_{\mathrm{in}} = 50{-}60$ V as seen in Fig. 6. That is, the voltage is low and the electrostatic force is weak; thus, some electrons are emitted into the atmosphere. However, this explanation is only a hypothesis and should be validated through further investigation. In the case of positive ions with a considerably greater mass and mobility less than those of electrons, C_{ion} increases at $V_{\mathrm{in}} = 60{-}80$ V and decreases at $V_{\mathrm{in}} = 80{-}100$ V although the data contain relatively large errors. Given that the ionic wind is induced by the collision between these drifting positive ions and the neutral particles, an increase in the ionic wind velocity at $V_{\mathrm{in}} = 60{-}100$ V should result in a corresponding increase in the C_{ion}. However, the decrease in C_{ion} at $V_{\mathrm{in}} = 80{-}100$ V is contrary to this explanation. Therefore, this decrease in C_{ion} is unlikely to be caused by electrical factors of discharge. Similar to the case of C_{O3}, this decrease in C_{ion} can result from dilution by air induced by the ionic wind, although C_{ion} increases with V_{in}. The C_{ion} of a positive ion is crucial in ionic wind generation.

4. Conclusion

In this study, a single MF-DBD plasma actuator is proposed, designed, and established with a simple and fundamental structure. Ionic wind velocity, temperature distribution, and ozone and ion concentrations are investigated to obtain the fundamental characteristics of the MF-DBD plasma actuator.

(1) NTP discharge is observed at input voltage $V_{\mathrm{in}} = 50{-}100$ V. NTP micro-discharges are generated from the edge surface of the MF toward the insulated electrode. The brightness and length of the NTP discharge increase with input voltage.
(2) The relationship between the input voltage V_{in} and the power consumption P_{con} at the high-voltage AC power supply is clarified. The relationship is approximated using a squared approximation.
(3) The waveforms of discharge voltage V_{dis} and current I_{dis} at $V_{\mathrm{in}} = 100$ V are obtained through measurements. Based on the waveform analysis, the positive values of the discharge current are higher than the negative absolute values. This phenomenon is consistent with the ionic wind generation mechanism.
(4) The time-dependent temperatures of NTP discharge T_{NTP} and MF T_{MF} are investigated. Simultaneously, a spike movement on the MF surface is also observed. Based on temperature analysis, natural convection occurs inside the MF, which suppresses the temperature increase in the MF by self-cooling.
(5) The effect of the input voltage V_{in} on ionic wind velocity u induced by the ionic wind is investigated experimentally. In addition, the relationship between the square root of the discharge current $\sqrt{I_{\mathrm{dis}}}$ and the wind velocity u is investigated. Their relationships are linear, and formulae of u are expressed as functions of V_{in}, V_{dis} (V_{RMS} and $V_{0\text{–}\mathrm{p}}$) and $\sqrt{I_{\mathrm{dis}}}$ from the experimental results. The characteristics of ion wind velocity with respect to the input voltage and discharge current are similar to those of the conventional DBD plasma actuator.
(6) The effect of the input voltage V_{in} on ozone concentration C_{O3} produced by NTP discharge is investigated. C_{O3} increases at $V_{\mathrm{in}} = 60{-}90$ V. C_{O3} is 140 ppm at $V_{\mathrm{in}} = 90$ V and decreases to 113 ppm at $V_{\mathrm{in}} = 100$ V. This decrease in ozone concentration can result from dilution by air induced by the ionic wind, although the concentration of C_{O3} increases with V_{in}.

The effect of the input voltage V_{in} on positive and negative ion concentrations C_{ion} generated by NTP discharge is investigated. The C_{ion} of negative ions is extremely low overall. The C_{ion} of positive ions increases at $V_{\mathrm{in}} = 60{-}80$ V and decreases at $V_{\mathrm{in}} = 80{-}100$ V. The characteristics of the discharge current waveform and the relationship between the discharge current and ion wind velocity are similar to those of conventional DBD plasma actuators. Therefore, the ionic wind generation mechanism in the MF-DBD plasma actuator is similar to that of the DBD plasma actuator.

Acknowledgment

The author would like to thank Mr. Hidenori Komuro, a student at Nippon Institute of Technology, for his contributions to the experiments.

References

[1] Kuwahara T., Fundamental characteristics of low-resistive particulate matter removal using a magnetic fluid and nonthermal plasma, *J. Magn. Magn. Mater.*, Vol. 498, 166161, 2020.

[2] Uehara S., Itoga T. and Nishiyama H., Discharge and flow characteristics using magnetic fluid spikes for air pollution control, *J. Phys. D: Appl. Phys.*, Vol. 48 (28), 282001, 2015.

[3] Yamamoto T., Mimura T., Otsuka N., Ito Y., Ehara Y. and Zukeran A., Diesel PM collection for marine and automobile emissions using EHD electrostatic precipitators, *IEEE Trans. Ind. Applicat.*, Vol. 46, pp. 1606−1612, 2010.

[4] Mizuno A., Electrostatic precipitation, *IEEE Trans. Electron Devices*, Vol. 7 (5), pp. 615−624, 2000.

[5] Hauksbee F., An experiment concerning the electricity of glass, discovering it self in an extraordinary manner, upon a smart attrition of it., *Physico-mechanical experiments on various subjects*: London (printed by R. Brugis), pp. 42−51, 1709.

[6] Robinson M., A history of the electric wind, *Am. J. Phys.*, Vol. 30 (5), pp. 366−372, 1962.

[7] Moreau E., Souakri S., Bellanger R. and Benard N., Ionic wind produced by a millimeter-gap DC corona discharge ignited between a plate and an inclined needle, *Int. J. Plasma Environ. Sci. Technol.*, Vol. 15 (1), e01001, 2021.

[8] Erfani R., Zare-Behtash H., Hale C. and Kontis K., Development of DBD plasma actuators: The double encapsulated electrode. *Acta Astronaut.*, Vol. 109, pp. 132−143, 2015.

[9] Likhanskii A. V., Shneider M. N., Macheret S. O. and Miles R. B., Modeling of dielectric barrier discharge plasma actuator in air, *J. Appl. Phys.*, Vol. 103 (5), 053305, 2008.

[10] Enloe C. L., McLaughlin T. E., Font G. I. and Baughn J. W., Parameterization of temporal structure in the single-dielectric-barrier aerodynamic plasma actuator, *AIAA J.*, Vol. 44 (6), pp. 1127−1136, 2006.

[11] Truong H. T., Uesugi Y. and Nguyen X. B., Mechanisms of low-frequency dielectric barrier discharge (DBD) plasma driven by unipolar pulses and bipolar pulses, *AIP Adv.*, Vol. 11 (2), 025022, 2021.

[12] Rodrigues F., Pascoa J. and Trancossi M., Heat generation mechanisms of DBD plasma actuators, *Exp. Therm. Fluid Sci.*, Vol. 90, pp. 55−65, 2018.

[13] Enloe C. L., McLaughlin T. E., VanDyken R. D., Kachner K. D., Jumper E. J. and Corke T. C., Mechanisms and responses of a single dielectric barrier plasma actuator: plasma morphology, *AIAA J.*, Vol. 42 (3), pp. 589−594, 2004.

[14] Kolbakir C., Hu H., Liu Y. and Hu H., An experimental study on different plasma actuator layouts for aircraft icing mitigation, *Aerosp. Sci. Technol.*, Vol. 107, 106325, 2020.

[15] Fujii K., Three flow features behind the flow control authority of DBD plasma actuator: Result of high-fidelity simulations and the related experiments, *Appl.Sci.*, Vol. 8 (4), 546, 2018.

[16] June M. S., Kribs J. and Lyons K. M., Measuring efficiency of positive and negative ionic wind devices for comparison to fans and blowers, *J. Electrostat.*, Vol. 69 (4), pp. 345−350, 2011.

[17] Huang Y., Li S., Zheng Q., Shen X., Wang S., Han P., Liu Z. and Yan K., Recent progress of dry electrostatic precipitation for PM2.5 emission control from coal-fired boilers, *Int. J. Plasma Environ. Sci. Technol*, Vol. 9 (2), pp. 69−85, 2015.

[18] Sato S., Furukawa H., Komuro A., Takahashi M. and Ohnishi N., Successively accelerated ionic wind with integrated dielectric-barrier-discharge plasma actuator for low-voltage operation, *Sci. Rep.*, Vol. 9 (1), 5813, 2019.

[19] Dragonas F. A., Neretti G., Sanjeevikumar P. and Grandi G., High-voltage high-frequency arbitrary waveform multilevel generator for DBD plasma actuators. *IEEE Trans. Ind. Applicat.*, Vol. 51 (4), pp. 3334−3342, 2015.

[20] Benard N. and Moreau E., Role of the electric waveform supplying a dielectric barrier discharge plasma actuator, *Appl. Phys. Lett.*, Vol. 100 (19), 193503, 2012.

[21] Cowley M. D. and Rosensweig R. E., The interfacial stability of a ferromagnetic fluid, *J. Fluid Mech.*, Vol. 30, pp. 671−688, 1967.

[22] Fukuda Y. and Douhara N., Study on interfacial phenomena of magnetic fluids. *JSME Int. J. Ser. B.*, Vol. 48, pp. 735−742, 2005.

[23] Piferi C., Barni R., Roman H. E. and Riccardi C., Current filaments in asymmetric surface dielectric barrier discharge, *Appl. Sci.*, Vol. 11 (5), 2079, 2021.

[24] Robinson M., Movement of air in the electric wind of the corona discharge, *Trans. Am. Inst. Electr. Eng.*, Part I: *Commun. Electron.*, Vol. 80 (2), pp. 143−150, 1961.

[25] Kiousis K. N., Moronis A. X. and Fylladitakis E. D., Ionic wind generation during positive corona discharge in a wire-cylinder air gap, *Int. J. Eng. Sci. Innov. Technol.*, Vol. 4 (1), pp. 229−239, 2015.

[26] Rafika M., Ramzi H. and Sassi B. N., A study of DC surface plasma discharge in absence of free airflow: ionic wind velocity profile. *J. Appl. Fluid Mech.*, Vol. 2 (2), pp. 43−48, 2012.

[27] Boeuf, J. P., Lagmich, Y., Callegari, T. and Pitchford, L., EHD force in dielectric barrier discharges parametric study and influence of negative ions., *Proc. 45th AIAA Aerospace Sciences Meeting and Exhibit*, Nevada, pp. 2170−2180, 2007.